Chinese Chemical Letters 34 (2023) 108148

Contents lists available at ScienceDirect

Chinese Chemical Letters

journal homepage: www.elsevier.com/locate/cclet

Covalent organic frameworks with imine proton acceptors for efficient photocatalytic H_2 production

Xiaolin Liu[a,1], Xiya Yang[a,1], Xu Ding[a], Hailong Wang[a,*], Wei Cao[b,*], Yucheng Jin[a], Baoqiu Yu[a], Jianzhuang Jiang[a,*]

[a] Beijing Advanced Innovation Center for Materials Genome Engineering, Beijing Key Laboratory for Science and Application of Functional Molecular and Crystalline Materials, Department of Chemistry and Chemical Engineering, School of Chemistry and Biological Engineering, University of Science and Technology Beijing, Beijing 100083, China
[b] State Key Laboratory of NBC Protection for Civilian, Beijing 102205, China

ARTICLE INFO

Article history:
Received 29 November 2022
Revised 24 December 2022
Accepted 11 January 2023
Available online 13 January 2023

Keywords:
Covalent organic framework
Photocatalysis
Hydrogen evolution reaction
Imine linkage
Protonation

ABSTRACT

Covalent organic frameworks (COFs) are promising crystalline materials for the light-driven hydrogen evolution reaction (HER) due to their tunable chemical structures and energy band gaps. However, deeply understanding corresponding mechanism is still challenging due to the multiple components and complicated electron transfer and reduction paths involved in photocatalytic HER. Here, the photocatalytic HER investigation has been reported based on three COFs catalysts, **1**–**3**, which are prepared by benzo[1,2-*b*:3,4-*b*':5,6-*b*']trithiophene-2,5,8-trialdehyde to react with C_3 symmetric triamines including tris(4-aminophenyl)amine, 1,3,5-tris(4-aminophenyl)benzene, and (1,3,5-tris-(4-aminophenyl)triazine, respectively. As the isostructural hexagonal honeycomb-type COF of **2** and **3** reported previously, the crystal structure of **1** has been carefully correlated through the powder X-ray diffraction study with the help of theoretical simulations. **1** shows highly porous framework with Brunauer-Emmett-Teller surface area of 1249 m^2/g. Moreover, the introduction of ascorbic acid into the photocatalytic system of COFs achieves the hydrogen evolution rate of 3.75, 12.16 and 20.2 mmol g^{-1} h^{-1} for **1**–**3**, respectively. The important role of ascorbic acid in photocatalysis of HER is disclosed to protonate the imine linkages of these COFs, leading to the obvious absorbance red-shift and the improved charge separation efficiency together with reduced resistance in contrast to pristine materials according to the spectroscopic and electronic characterizations. These innovations of chemical and physical properties for these COFs are responsible for their excellent photocatalytic performance. These results elucidate that tiny modifications of COFs structures is able to greatly tune their band structures as well as catalytic properties, therefore providing an available approach for optimizing COFs functionalities.

Covalent organic frameworks (COFs) are those crystalline organic materials prepared by covalent-bonded discrete building blocks [1–3]. The highly porous and functional COFs enable the diverse functionalities including as gas separation and storage [4–8], electronics [9–11] and catalysis [12–15]. COFs further extend the organic materials scopes into a new class of crystalline two- and three-dimensional (2D, 3D) well-defined porous frameworks [16–20]. In particular, those 2D COFs are able to exhibit unique photonic and electronic properties relative to discrete molecular modules and amorphous polymers [21–25]. The integration of various aromatic building blocks into polymeric π-conjugated backbones is regarded to generate a new kind of semiconductors with adjustable electronic structures. The unique semiconductive properties of COFs make them as interesting materials for photocatalysis of hydrogen evolution and carbon dioxide reduction reactions [13,22,23].

Solar-driven hydrogen evolution from water is a promising approach to provide clean energy for the replacement of fossil energy [26,27]. In this direction, efficient photocatalysts are highly desired to have comprehensive characteristics covering light capture, exciton transport, charge separation, and surface redox reaction [28,29]. A large number of active photocatalysts such as oxide semiconductors [30–32], metal-organic frameworks [33–37] and COFs [38–41] have been demonstrated to generate hydrogen under visible light irradiation. Various COFs systems made up of diverse

* Corresponding authors.
E-mail addresses: hlwang@ustb.edu.cn (H. Wang), vic_cw@126.com (W. Cao), jianzhuang@ustb.edu.cn (J. Jiang).
[1] These authors contributed equally to this work.

https://doi.org/10.1016/j.cclet.2023.108148
1001-8417/

chromophores such as pyrene (Py) [42], thiazolo-[5,4-*d*]thiazole (TTz) [43], triazine (Tz) [44,45] and dibenzo[b,d]thiophene sulfone (DBTP) units [46] have been demonstrated to exhibit excellent photocatalytic activity towards hydrogen evolution reaction (HER) with the help of Pt cocatalyst in presence of sacrificial reagents [27,47]. The post-modification of COFs enables the adjustment of their electronic structures for efficient photocatalysis of HER. However, deeply understanding corresponding mechanism is still necessary yet challenging due to the multiple components and complicated electron transfer and reduction path involved in photocatalysis.

In this study, a new two-dimensional COF, named **1**, has been prepared based on the imine-bonded polymerization of benzo[1,2-*b*:3,4-*b*':5,6-*b*"]trithiophene-2,5,8-tricarbaldehyd (BTT) with tris(4-aminophenyl)amine (TAPA). The photocatalytic performance of **1** has been investigated towards HER, in comparison with COFs analogues **2** and **3** prepared by BTT condensing with 1,3,5-tris-(4-aminophenyl)triazine (TAPT) and 1,3,5-tris(4-aminophenyl)benzene (TAPB), respectively. It is worth noting that BTT derivatives have drawn considerable attention owing to its adjustable energy levels, optical band gaps, and relatively high hole mobility, which is widely used in the fields of solar cells and organic catalysis [15,48,49]. Certainly, corresponding semiconductor properties could be tuned via the polymerization with different C_3 symmetrical building blocks to generate COFs. The protonation effect of imine COFs in the presence of ascorbic acid (Aa) on photocatalysis of HER has been disclosed. The electronic structures and charge separation efficiency of COFs have been tuned, leading to the different photocatalytic behaviors, in terms of hydrogen evolution rate. In particular, **3** has the rapid hydrogen production speed, namely 20.2 mmol g^{-1} h^{-1}. These results disclose that the electronic structures and properties of active COFs are different from pristine species during photocatalysis, giving a hint to employ the interesting dynamic characteristics of these active catalysts for diverse applications.

In the present case, **1** with designed hexagonal framework was fabricated through the polymerization of TAPA and BTT under solvothermal condition (Fig. 1a). Its isostructral COFs, **2** and **3**, have also been prepared using the reported methods [48,49]. The integration of BTT and complementary monomers with both big conjugation systems into COFs may effectively tune the band gaps of these polymeric materials towards efficient visible light-driven photocatalysis of HER. The excellent crystallinity of the newly prepared COF (**1**) together with its porous architecture, was disclosed through a series characterization methods including powder X-ray diffraction (PXRD), gas sorption, and transmission electron microscopy (TEM). PXRD data for **1** had the sharp diffraction signals at 5.38°, 9.34°, 14.23°, 19.30° and 25.83° (Fig. 1b), which come from the reflections of (100), (210), (230), (340) and (001) planes, respectively, in the hexagonal lattice. Referring to the hexagonal architectures of **2** and **3** prepared by two C_3 symmetric building blocks [48,49], **1** should be their isostructural analogue. As a result, a structural model with hexagonal system and space group of *P*6 was proposed for **1**, showing an AA stacking according to the density functional tight binding (DFTB) method (Fig. 1e). The PXRD data and structural model of **1** were further checked using the Pawley refinement. The small fitting values of $R_{wp} = 4.20\%$ and $R_p = 3.02\%$ directly reflected the good crystallinity and the right structural model for **1**. For **2** and **3**, their purities were also determined by the PXRD and Pawley refinements (Figs. 1c–g).

The nitrogen (N_2) sorption measurements at 77 K were done over **1**–**3** activated under the highly degassing conditions at 120 °C. The adsorption curves of these three COFs follow the good type-I configuration (Fig. 2a), revealing their micropores nature enclosed by two kinds of molecular modules. As shown in Fig. 2b, a narrow pore size distribution of **1**–**3** was found at 1.10, 1.27 and 1.27 nm, respectively. These experimental pore sizes of **1**–**3** is well matching with corresponding data determined from the structural models. The Brunauer-Emmett-Teller (BET) surface area of **1**–**3** were calculated to be 1249, 1433 and 1387 m^2/g, respectively. In comparison with **2** and **3**, the smaller BET surface area of **1** is due to the short TAPA building block used.

The conversion of reactive amine and aldehyde groups to imine linkage together with chemical structure integrity of framework for **1**–**3** were qualitatively examined by Fourier transform infrared spectra (FTIR) and solid-state ^{13}C cross-polarization magic angle spinning nuclear magnetic resonance (^{13}C NMR) spectroscopy. The FTIR spectra of **1** and its monomers showed nearly disappearance for C=O stretching signal at 1661 cm^{-1}. It is also true for the amino group signal at 3200–3400 cm^{-1} for amine and aldehyde compounds (Fig. 2c). The new observation of a band at 1611 cm^{-1} was assigned to C=N stretching band. These data revealed the conversion of monomers to form imine connection [50]. The formation of imine linkages in **1** was further proven by the appearance of 156 ppm in its ^{13}C NMR spectrum (Fig. S1 in Supporting information). This point was also supported by the signals of imine carbon atoms of **2** and **3** in the ^{13}C NMR spectra (Figs. S2 and S3 in Supporting information). The FTIR and ^{13}C NMR spectra of **2** and **3** are consistent with those characteristic signals previously reported (Figs. S4 and S5 in Supporting information) [48,49]. The morphology of **1** exhibited the layered structure according to SEM and TEM photos (Figs. 2d and e). The high resolution transmission electron microscopy (HRTEM) picture of **1** was determined (Fig. 2f). The lattice fringes of **1** with the distance of 0.36 nm were clearly observed, consistent with the interlayered separation, namely the (001) plane, in the distance of 0.35 nm. Energy-dispersive spectroscopy (EDS) photos revealed the carbon, nitrogen, and sulfur elements in **1** (Fig. S8 in Supporting information). Those are also true for **2** and **3** (Figs. S6, S7, S9 and S10 in Supporting information). Thermogravimetric (TG) analysis was performed in nitrogen atmosphere. The TG curves determined the decomposed temperature of **1**–**3** in the range of 513–550 °C (Fig. S11 in Supporting information), indicating the good thermal stability for these COFs.

The UV–vis diffuse reflectance spectra (DRS) of **1**–**3** displayed a broad harvesting scope with maximum peaks at 540, 468 and 462 nm respectively, in the visible region (Fig. 3a). The optical band gaps (E_g) values of **1**–**3** were inferred to 1.92, 2.18 and 2.18 eV, respectively. This clearly discloses the semiconductor characteristic of those COFs, also illustrating the narrower band gap for **1** relative to those of **2** and **3** (Fig. 3b). This is supported by the observation of carmine power of **1** sample, orange and bronze power for **2** and **3**, respectively. To deeply disclose the electronic structures of the three COFs, Mott-Schottky curves of three COFs were collected under three different frequencies to determine their conduction band (CB) potentials. The positive Mott-Schottky fitting plots for all **1**–**3** showed the positive slopes values, indicating the n-type semiconductor attribution for these three compounds. The CB potential of **1** was estimated to be −1.22 V *vs.* NHE. Instead of C_3 building block TAPA in **1**, the introduction of TAPT and TAPB into **2** and **3** rose the COFs CB potentials to −1.29 and −1.27 V (Fig. 3c, Figs. S12 and S13 in Supporting information), respectively. Furthermore, on the basis of equation $E_{CB} = E_{VB} - E_g$, the valence band (VB) potentials of **1**–**3** was determined to be 0.70, 0.89 and 0.90 V *vs.* NHE (Fig. 3d), Obviously, those COFs should have much more negative CB potentials than the water reduction potential (0 V *vs.* NHE), thermodynamically enabling the proton reduction from water [51].

The visible light-driven HER activities of three COFs were explored with the help of sacrificial reagent and Pt cocatalyst upon $\lambda \geq 420$ nm light irradiation. Significantly, **1** was able to exhibit the H_2 evolution speed of 3.75 mmol g^{-1} h^{-1} in the presence of Aa during 4 h photocatalysis. Under the same conditions, **2** and **3** showed the much higher HER rate of 12.16 and 22.02 mmol g^{-1}

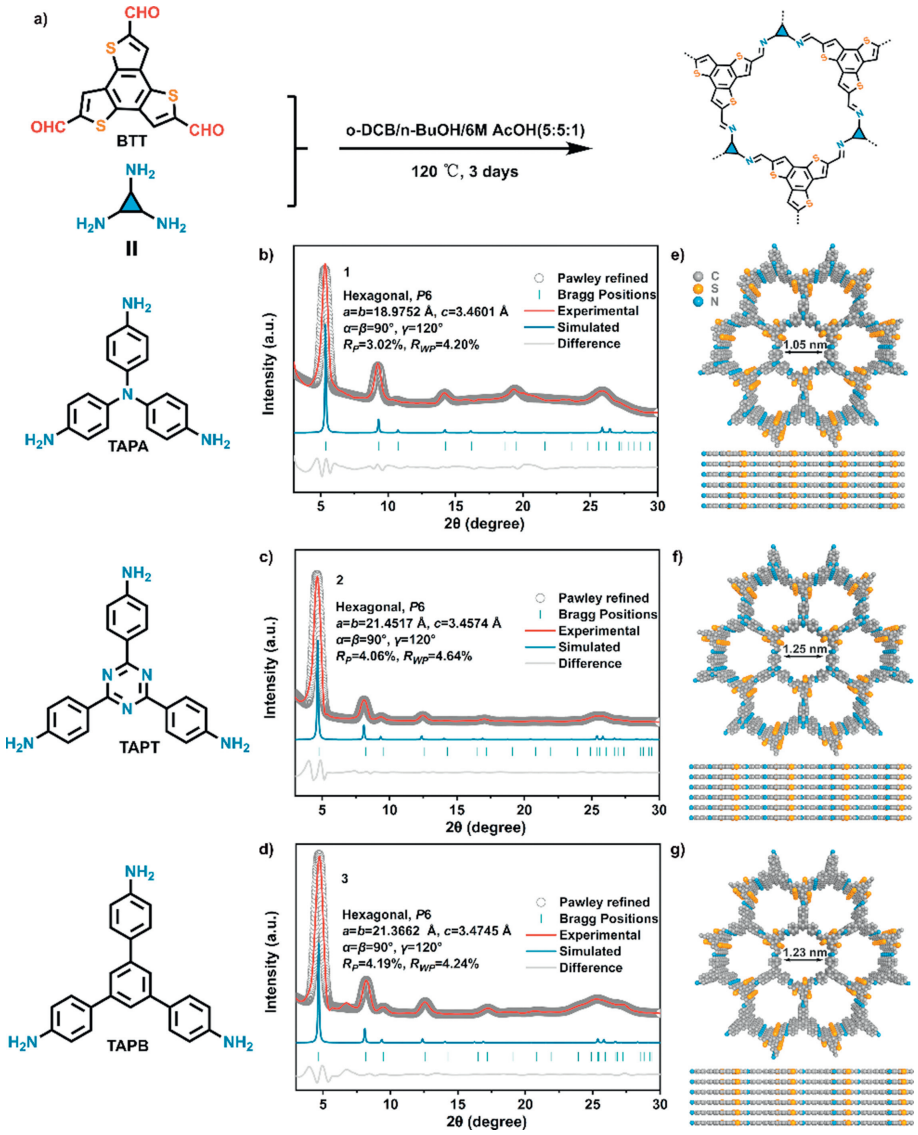

Fig. 1. (a) Synthesis of **1**–**3**. (b-d) Experimental, Pawley refined, and simulated PXRD patterns as well as the difference plots for **1**–**3**. (e-g) Top and side views of the simulated packing structure of **1**–**3** (Hydrogen atoms are not shown in these structures).

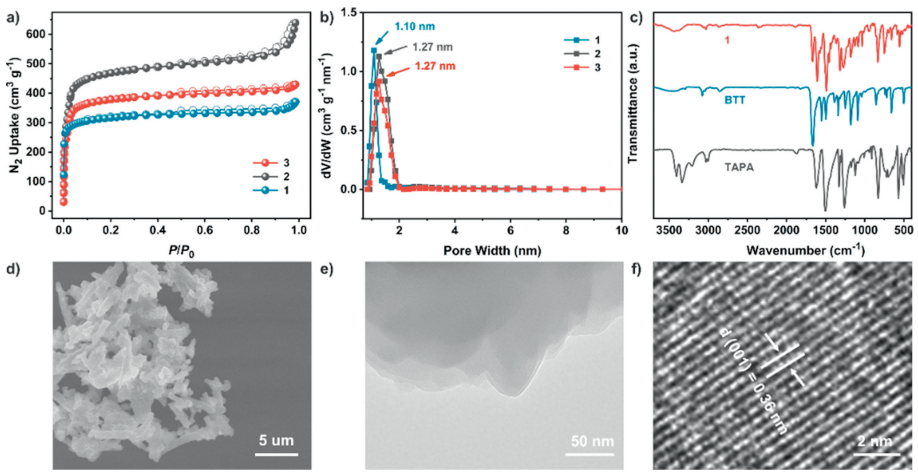

Fig. 2. (a) N_2 adsorption (solid) and desorption (hollow) curves of **1**–**3** at 77 K. (b) Pore-size distributions of **1**–**3**. (c) FTIR curves of BTT, TAPB and **1**. (d-f) SEM, TEM, and HRTEM image for **1**.

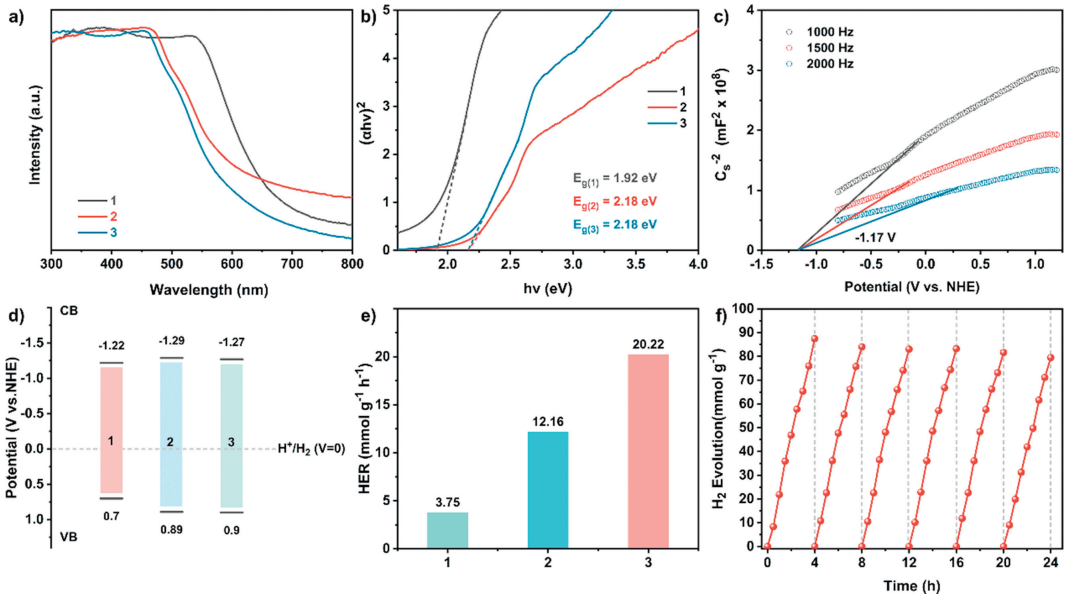

Fig. 3. (a) UV–vis diffuse reflectance spectra and (b) Tauc plots of **1**–**3**. (c) Mott-Schottky plots of 3 in 0.1 mol/L Na_2SO_4 aqueous solution at frequency of 1000, 1500 and 2000 Hz. (d) Band structure diagram and (e) photocatalytic H_2 evolution activities of **1**–**3**. (f) Recyclability test of **3**. Photocatalysis system: 5.0 mg COF, H_2PtCl_6 (8.0 wt% Pt based on COF mass), 0.1 mol/L Aa, 20.0 mL of H_2O, light $\lambda \geq 420$ nm.

h^{-1} (Fig. 3e), respectively. Notably, the hydrogen evolution rate for **3** is comparable to those for excellent COF photocatalysts (Table S1 in Supporting information) [22,30,46,52]. Subsequently, a long-term photocatalytic activity of **3** for H_2 production was studied using the above system. As displayed in Fig. 3f, a tiny attenuation was observed in lasting six-time cycling photocatalytic H_2 production tests for **3**. The recycled COF was subjected to the characterizations again including FTIR spectra, TEM, and EDS mapping, Fig. S14 and S15, illustrating there were none remarkable changes in compositions and morphologies of COF sample before and after the cycling photocatalysis. In contrast to Aa, the employment of triethanolamine and sodium ascorbate as sacrificial reagents only led to the trace amount of hydrogen under the similar HER conditions, indicating the important role of sacrificial reagents in the present photocatalysis.

It is worth noting that the color of **1**–**3** samples are significantly changed during photocatalytic process, implying the fact that the active working COFs are different from the pristine species (Figs. S16 and S17 in Supporting information). Comparative study in COFs samples, **1**-Aa, **2**-Aa and **3**- Aa, immersed in Aa aqueous solution used in photocatalytic system and as-prepared samples were explored, and their remarkable activity for HER associated with the introduction of Aa (Fig. S18 in Supporting information). **1**-Aa, **2**-Aa and **3**-Aa showed the changed color, supporting the hypothesis about the protonation of imine units in these COFs. To provide a clear insight to protonation effect on COFs, a series of measurements were performed on **1**-Aa, **2**-Aa and **3**-Aa in the comparison with as-prepared COFs. UV–vis diffuse reflectance spectroscopic results of **1** and **1**-Aa confirmed the broaden visible light absorption scope for the latter sample (Fig. S19a in Supporting information). The similar phenomena were also observed in the study in **2** *vs.* **2**-Aa and **3** *vs.* **3**-Aa, Figs. S20a and S21a. These results, compared with the electronic absorption of Aa in the UV region, further indicated the change of above visible light absorption scopes for COFs associated with the immersion in Aa (Fig. S22 in Supporting information) [53]. Furthermore, the band gaps of **1**-Aa, **2**-Aa and **3**-Aa derived from Tauc plots were 1.38, 2.01 and 1.86 eV (Fig. 4a, Figs. S19b and S20b in Supporting information), respectively, smaller than those for **1**–**3**. According to the above mentioned methods, CB and VB values of **1**-Aa, **2**-Aa and **3**-Aa were determined as −1.29&0.09, −1.34&0.67, and −1.38&0.48 V *vs.* NHE (Fig. S23 in Supporting information), respectively. It has been demonstrated that the narrow band gap is beneficial for the broader absorption of in the solar spectrum as well as the decrease of the electron-hole recombination rate [54,55], thus improving the catalytic performance [56]. In addition, the most negative CB potential *vs.* NHE of **3**-Aa among three catalysts should be favorable for its highest H_2 evolution activity [57].

Furthermore, the charge separation efficiency was investigated. In contrast to **1**, the protonated **1**-Aa had a bigger photocurrent (Fig. S24 in Supporting information), indicating the enhanced charge separation efficiency for the latter species. The similar phenomena were also observed in the photocurrent response curves for **2**, **3**, **2**-Aa and **3**-Aa (Fig. 4b and Fig. S25 in Supporting information). In addition, the electrochemical impedance spectra (Fig. 4c, Figs. S26 and S27 in Supporting information) show that **1**-Aa, **2**-

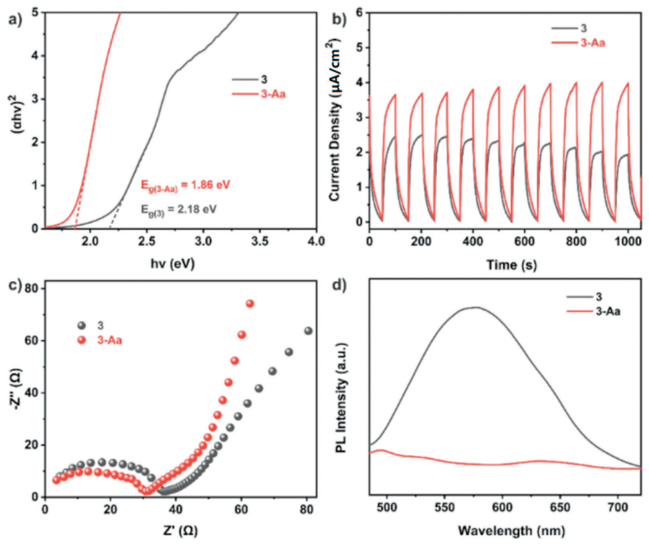

Fig. 4. (a) Tauc plots of **3** and **3**-Aa. (b) *I-t* diagrams ($\lambda \geq 420$ nm) and (c) EIS of **3** and **3**-Aa. (d) The PL spectra of **3** and **3**-Aa in water.

Aa and **3**-Aa have smaller semicircle radius relative to corresponding pristine COFs, proving their lower charge transfer resistance after protonation. The photocurrent diagram reveals the best charge separation efficiency for **3**-Aa at the first 5-circle test (Fig. S28 in Supporting information). In addition, **3**-Aa shows the slightly smaller resistance than the other species according to electrochemical impedance results (Fig. S29 in Supporting information). These results are responsible for the superior photocatalytic HER property for **3** in the presence Aa. After protonation of **1**–**3**, their emission was completely quenched for the formed **1**-Aa, **2**-Aa and **3**-Aa (Fig. 4d and Fig. S30 in Supporting information), also implying the enhanced charge separation and transfer.

Density functional theory (DFT) calculations based on cluster models have been conducted on **3** and **3**-Aa with the most excellent photocatalysis behaviours, in order to give an additional theoretical evidence. The corresponding models were denoted as **3**(M) and **3**-Aa(M) (details in Figs. S31 and S32 in Supporting information) [53]. Using PBE0 [58], protonated imine groups on the framework of **3**(M) to form **3**-Aa(M) significantly decreases the HOMO-LUMO gap from 3.68 eV to 0.55 eV. The transition energy levels and probabilities were simulated by time-dependent DFT, to pursue the rational explanation for changed UV–vis data. The smallest excitation energy of **3**(M) displayed the non-vanishing oscillator strength of 3.02 eV, leading to the electronic absorption of 411 nm. In contrast, the protonated **3**-Aa(M) had a reduced lowest excitation energy of 2.14 eV (corresponding to 580 nm) (Fig. S33 in Supporting information). The well consistency between the theoretical and observed red-shift conclusions further illustrate the protonation effect of imine COFs.

In summary, the photocatalytic activities of three COFs analogues towards HER have been explored, exhibiting the excellent hydrogen evolution rate. The imine units of these COFs are able to accept protons to generate protonated species, tuning the intrinsic electronic structures and charge separation efficiency. This study not only provides the new HER photocatalysts, but also elucidates the electronic structures change of working COFs photocatalysts during the photocatalysis, different from pristine materials. The related results are helpful for the field of COF catalysis.

Declaration of competing interest

The authors declare that they have no known competing financial interests or personal relationships that could have appeared to influence the work reported in this paper.

Acknowledgments

This work was financially supported by the Natural Science Foundation of China (Nos. 22235001, 22175020, 22131005 and 21631003), Xiaomi Young Scholars Program, the Fundamental Research Funds for the Central Universities, and University of Science and Technology Beijing.

References

[1] A.P. Côté, A.I. Benin, N.W. Ockwig, et al., Science 310 (2005) 1166–1170.
[2] C.S. Diercks, O.M. Yaghi, Science 355 (2017) eaal1585.
[3] K. Geng, T. He, R. Liu, et al., Chem. Rev. 120 (2020) 8814–8933.
[4] Y. Han, Q. Zhang, N. Hu, et al., Chin. Chem. Lett. 28 (2017) 2269–2273.
[5] F. Jin, E. Lin, T. Wang, et al., J. Am. Chem. Soc. 144 (2022) 5643–5652.
[6] X.H. Han, K. Gong, X. Huang, et al., Angew. Chem. Int. Ed. 61 (2022) e202202912.
[7] M. Liu, Y.J. Chen, X. Huang, et al., Angew. Chem. Int. Ed. 61 (2022) e202115308.
[8] Z. Wang, S. Zhang, Y. Chen, et al., Chem. Soc. Rev. 49 (2020) 708–735.
[9] X. Liu, D. Huang, C. Lai, et al., Chem. Soc. Rev. 48 (2019) 5266–5302.
[10] S. Li, Y. Liu, L. Dai, et al., Energy Storage Mater. 48 (2022) 439–446.
[11] A. Halder, M. Ghosh, A. Khayum M, et al., J. Am. Chem. Soc. 140 (2018) 10941–10945.
[12] H.C. Ma, G.J. Chen, F. Huang, et al., J. Am. Chem. Soc. 142 (2020) 12574–12578.
[13] Y.R. Wang, H.M. Ding, X.Y. Ma, et al., Angew. Chem. Int. Ed. 61 (2022) e202114648.
[14] B. Han, X. Ding, B. Yu, et al., J. Am. Chem. Soc. 143 (2021) 7104–7113.
[15] J. Jeon, Y.J. Kim, S.H. Joo, et al., Angew. Chem. Int. Ed. 62 (2023) e202217416.
[16] X. Guan, F. Chen, Q. Fang, et al., Chem. Soc. Rev. 49 (2020) 1357–1384.
[17] X. Liu, Y. Jin, H. Wang, et al., Adv. Mater. (2022) 2203605.
[18] H. Ding, J. Li, G. Xie, et al., Nat. Commun. 9 (2018) 5234.
[19] Z. Shan, M. Wu, D. Zhu, et al., J. Am. Chem. Soc. 144 (2022) 5728–5733.
[20] R. Sun, X. Wang, X. Wang, et al., Angew. Chem. Int. Ed. 61 (2022) e202117668.
[21] Y. Zhi, Z. Wang, H.L. Zhang, et al., Small 16 (2020) 2001070.
[22] W. Li, X. Ding, B. Yu, et al., Adv. Funct. Mater. (2022) 2207394.
[23] L. Sun, M. Lu, Z. Yang, et al., Angew. Chem. Int. Ed. 61 (2022) e202204326.
[24] S. Yang, R. Sa, H. Zhong, et al., Adv. Funct. Mater. 32 (2022) 2110694.
[25] B. Zhao, X. Lu, Q. Wang, et al., Chin. Chem. Lett. 31 (2022) 831–835.
[26] L. Chen, M. Huang, B. Chen, et al., Chin. Chem. Lett. 33 (2022) 2867–2882.
[27] B. Xu, S. Qi, M. Jin, et al., Chin. Chem. Lett. 30 (2019) 2053–2064.
[28] H. Wang, H. Wang, Z. Wang, et al., Chem. Soc. Rev. 49 (2020) 4135–4165.
[29] Q. Wang, K. Domen, Chem. Rev. 120 (2020) 919–985.
[30] C.C. Li, M.Y. Gao, X.J. Sun, et al., Appl. Catal. B 266 (2020) 118586.
[31] S. Ida, K. Sato, T. Nagata, et al., Angew. Chem. Int. Ed. 57 (2018) 9073–9077.
[32] Y. Zhang, Z. Liu, C. Guo, et al., Catal. Sci. Technol. 12 (2022) 4535–4543.
[33] W. Wang, X. Xu, W. Zhou, et al., Adv. Sci. 4 (2017) 1600371.
[34] H. Liu, C. Xu, D. Li, et al., Angew. Chem. Int. Ed. 57 (2018) 5379–5383.
[35] G. Lan, Y.Y. Zhu, S.S. Veroneau, et al., J. Am. Chem. Soc. 140 (2018) 5326–5329.
[36] Y. Lu, H. Zhong, J. Li, et al., Angew. Chem. Int. Ed. (2022) e202208163.
[37] R.B. Lin, Z. Zhang, B. Chen, Acc. Chem. Res. 54 (2021) 3362–3376.
[38] Z. Mi, T. Zhou, W. Weng, et al., Angew. Chem. Int. Ed. 60 (2021) 9642–9649.
[39] C. Li, S. Cao, J. Lutzki, et al., J. Am. Chem. Soc. 144 (2022) 3083–3090.
[40] S. Zhang, G. Cheng, L. Guo, et al., Angew. Chem. Int. Ed. 59 (2020) 6007–6014.
[41] C. Lin, C. Han, L. Gong, et al., Catal. Sci. Technol. 11 (2021) 2616–2621.
[42] W. Li, X. Huang, T. Zeng, et al., Angew. Chem. Int. Ed. 60 (2021) 1869–1874.
[43] L. Guo, Y. Niu, S. Razzaque, et al., ACS Catal. 9 (2019) 9438–9445.
[44] L. Zhang, Y. Zhang, X. Huang, et al., Chem. Sci. 13 (2022) 8074–8079.
[45] S. Li, M.F. Wu, T. Guo, et al., Appl. Catal. B 272 (2020) 118989.
[46] X. Wang, L. Chen, S.Y. Chong, et al., Nat. Chem. 10 (2018) 1180–1189.
[47] R.J. Katz, M.J. Theibault, N.E. Kirchner-Hall, et al., Adv. Energy Mater. (2022) 2201869.
[48] H. Wei, J. Ning, X. Cao, X. Li, et al., J. Am. Chem. Soc. 140 (2018) 11618–11622.
[49] Z. Li, Z. Zhang, R. Nie, et al., Adv. Funct. Mater. 32 (2022) 2112553.
[50] S. Kandambeth, V. Venkatesh, D.B. Shinde, et al., Nat. Commun. 6 (2015) 6786.
[51] S. Wei, F. Zhang, W. Zhang, et al., J. Am. Chem. Soc. 141 (2019) 14272–14279.
[52] R. Chen, Y. Wang, Y. Ma, et al., Nat. Commun. 12 (2021) 1354.
[53] J. Yang, A. Acharjya, M.Y. Ye, et al., Angew. Chem. Int. Ed. 60 (2021) 19797–19803.
[54] C. Tian, Y. Liang, W. Chen, et al., Phys. Chem. Chem. Phys. 22 (2020) 1841–1846.
[55] M.S. Seyed Dorraji, M.H. Rasoulifard, Z. Aghamoradi, et al., J. Photochem. Photobiol. A 394 (2020) 112486.
[56] S. Bolar, S. Shit, N.C. Murmu, et al., ACS Appl. Mater. Interfaces 13 (2021) 765–780.
[57] Z. Zhao, X. Chen, B. Li, et al., Adv. Sci. 9 (2022) 2203832.
[58] C. Adamo, V. Barone, J. Chem. Phys. 110 (1999) 6158–6170.